



Characterization and Properties of CuZrAlTiNiSi High Entropy Alloy Coating Obtained By Mechanical Alloying and Vacuum Hot-Pressing Sintering

ZIHAN HAN,¹ DONGZHI WANG,^{1,2} XIAOHAN CHEN,¹
GUOMANG SHAO,¹ XI ZHANG,¹ WENJUAN GE,¹
and YAN WANG^{1,3}

1.—School of Materials Science and Engineering, University of Jinan, No. 336, West Road of Nan Xinzhuang, Jinan 250022, People's Republic of China. 2.—e-mail: mse_wangdz@ujn.edu.cn. 3.—e-mail: mse_wangy@ujn.edu.cn

The CuZrAlTiNiSi high entropy alloy coating (HEAC) was synthesized on T10 substrate using mechanical alloying and vacuum hot-pressing sintering technique. The results show that the final product of as-milled powders is amorphous HEA phase with homogeneous component distribution. The sintered coating is composed of solid solutions and intermetallic compounds. No pores and defects appear in the HEAC surface, suggesting a good consolidation quality. In addition, the HEAC possesses a good interface bonding, mainly owing to the diffusion of Al atoms from coating to substrate. The average microhardness of the coating reaches 927 HV_{0.2}, and is more than 3 times higher than the substrate (281 HV_{0.2}). The high microhardness can be mainly explained by the second phase strengthening effect and solid-solution strengthening. Furthermore, compared with the substrate, the HEAC exhibits excellent wear resistance with lower friction coefficient, reduction of the wear groove depths and widths, fewer wear volumes, and minimum specific wear rate under the same conditions. Moreover, based on the wider passive region and uniform surface corrosion morphology, the HEAC presents a good pitting resistance in seawater solution.

INTRODUCTION

The surface modification of metallic materials is a hotspot in material manufacture and performance development. The coating can not only realize the recycle application of the substrate but also improve the surface properties of the substrate materials.

High entropy alloys (HEAs) as a new concept of alloy systems have attracted extensive research attention. Compared with traditional alloys, HEAs are usually composed of multiple principal elements with equiatomic or near-equiatomic concentrations.¹ Due to their unique solid solution structures, HEAs reveal a variety of interesting and unusual properties, such as high hardness and strength, high wear resistance, and good corrosion resistance.^{2–5} Therefore, HEAs are the suitable candidates as coating materials by virtue of their excellent surface properties.

Al₂CrFeNiCoCuTi_x and CoCrCuFeNiNb HEA coatings (HEACs) with excellent corrosion resistance and good wear resistance were prepared by laser cladding and plasma transferred arc cladding,^{6,7} respectively. TiTaHfNbZr HEA thin films were deposited on biomedical Ti6Al4V substrates by RF magnetron sputtering, which provided a significantly enhanced surface protection against wear and cracking.⁸

The vacuum hot-pressing sintering (VHPS) process accompanied by heating and pressing at the same time, is beneficial to the powder particle contact, adequate atomic diffusion and high densification. The grain refinement and compact structure as well as excellent performances can be easily acquired by the VHPS technique. Recently, there have been several reports about HEACs fabricated by VHPS as an effective and convenient technology for coating preparation.^{9,10} The VHPS-ed

CoCrFeNiW and CoCrFeNiW_{0.5}Mo_{0.5} HEACs on Q235 steel substrates exhibited superior wear resistance and corrosion resistance.¹⁰

In this study, CuZrAlTiNiSi coating powders were synthesized by the mechanical alloying (MA) technique. Then, we successfully fabricated HEACs with good sintering quality on T10 steel substrate by the VHPS technique. Moreover, the microstructures, microhardness, and wear and corrosion resistance of the HEACs were investigated.

EXPERIMENTAL

Cu, Zr, Al, Ti, Ni and Si element powders ($\sim 70 \mu\text{m}$ of particle size and $> 99.5 \text{ wt.}\%$ of purity) with equiatomic composition were mechanically alloyed to prepare CuZrAlTiNiSi HEA powders using a planetary ball mill (KE-2L) at 350 rpm in an argon atmosphere. High-performance stainless-steel vials and balls were utilized, and the ball-to-powder mass ratio was 15:1.

T10 steel was used as the substrate, and its composition is shown in Supplementary Table I. The substrate surface with 20 mm diameter was ground with 400-, 1000- and 2000-grit SiC abrasive papers in turn, followed by polishing to a mirror using a polishing machine (P-2; LunJie, Shanghai, China) with Cr₂O₃ and Al₂O₃ as abrasives. The processed T10 steel was put into a graphite mold, and then the as-milled CuZrAlTiNiSi HEA powders were directly superposed to the mirror side of substrate. The graphite mold equipped with the samples was put into a VHPS furnace (ZT-70-20Y) with $3 \times 10^{-3} \text{ Pa}$ of vacuum. A hot-pressing process was conducted to 930°C at a heating rate of 5°C/min, under a pressure of 30 MPa with 30 min holding time.

The phase analyses of the as-milled powders and coating were examined by x-ray diffraction (XRD; Rigaku D8 Advance) in Bragg-Brentano geometry using Cu K α radiation ($\lambda = 0.15406 \text{ nm}$). The acceleration voltage and current were set to 40 kV and 30 mA, respectively. The thermal behaviors of the as-milled powders were determined by differential scanning calorimetry (DSC) at a heating rate of 20 K/min. The microstructure and chemical composition were investigated by field emission scanning electron microscopy (FESEM; QUANTA FEG 250, FEI, USA) coupled with energy dispersive spectrometry (EDS; Oxford Instruments, UK; X-Max 50 mm²). The microhardness of the coating was measured by a Microscopy/Vickers hardness tester (HV-1000), with a load of 200 g and a duration time of 15 s. Dry sliding wear tests of the samples were performed on a linearly reciprocating friction and wear tester (RTEC MFT-50) in the ball-on plate configuration. A GCr15 steel ball with a diameter of 6 mm and mass (m_0) of 0.9216 g was used as grinding material which was undertaken through heat treatment. Moreover, the stroke length, normal load, frequency, and duration time were

4.5 mm, 60 N, 4 Hz, and 15 min, respectively. Afterwards, a white light interference device (USP-Sigma) was carried out to measure the three-dimensional (3D) topography of the scratch in the worn samples, and then the wear volume was obtained. In order to be sufficient to capture the wear response, the ring-disk friction and wear tests were carried out. The relevant test conditions are displayed in the supplementary file.

The corrosion behaviors of the HEAC and substrate were studied by an electrochemical polarization measurement using an electrochemical workstation (CHI660E) in an artificial seawater solution at ambient temperature. The tested samples were used as a working electrode, a platinum sheet was used as a counter electrode, and Ag-AgCl was used as a reference electrode. The potential sweep rate was 3.0 mV/s.

RESULTS AND DISCUSSION

Figure 1a shows XRD patterns of CuZrAlTiNiSi HEA powders after different milling time. The diffraction peaks of all the HEA pure elements can be observed in the initial mixing powders (0 h). After 5 h of MA, the as-milled products are still the mixture phases of the starting elemental powders, and alloying the alloy between the principal elements does not occur. However, the diffraction peaks obviously broaden and their intensities decrease. As the milling time increases to 15 h, some diffraction peaks of the principal element phase begin to disappear, indicating the existence of alloying behavior. After 35 h, a pronounced smooth hump appears, presenting the formation of amorphous phase. Even when the milling time increases to 125 h, the amorphous HEA phase still exists, showing better mechanical stability during the milling process. The 125-h milled amorphous HEA powders have been used as coating powders in the present study.

Figure 1b and c presents the DSC curves of the as-milled powders (125 h) in two characteristic temperature intervals. As shown in Fig. 1b, the two exothermic peaks further verify the formation of an amorphous phase, and indicate its two-stage crystallization behavior. The formation of the CuZrAlTiNiSi HEA amorphous phase during MA can be described by the following stages.¹¹ The principal element powders tend to agglomerate to form larger composite particles with a layer structure in the initial MA process. With the development of MA, the number of layers of powder particles and interfaces increased. Then, naturally multilayered composite particles can be formed under continuously intensive impacts and shear forces. Finally, increasing the MA time leads to solid-state diffusion at the clean metallic interfaces and gradually decreases the free energy. At the same time, ball milling introduces massive lattice imperfections, which enhance the atomic diffusion between the principal elements. The amorphization via MA

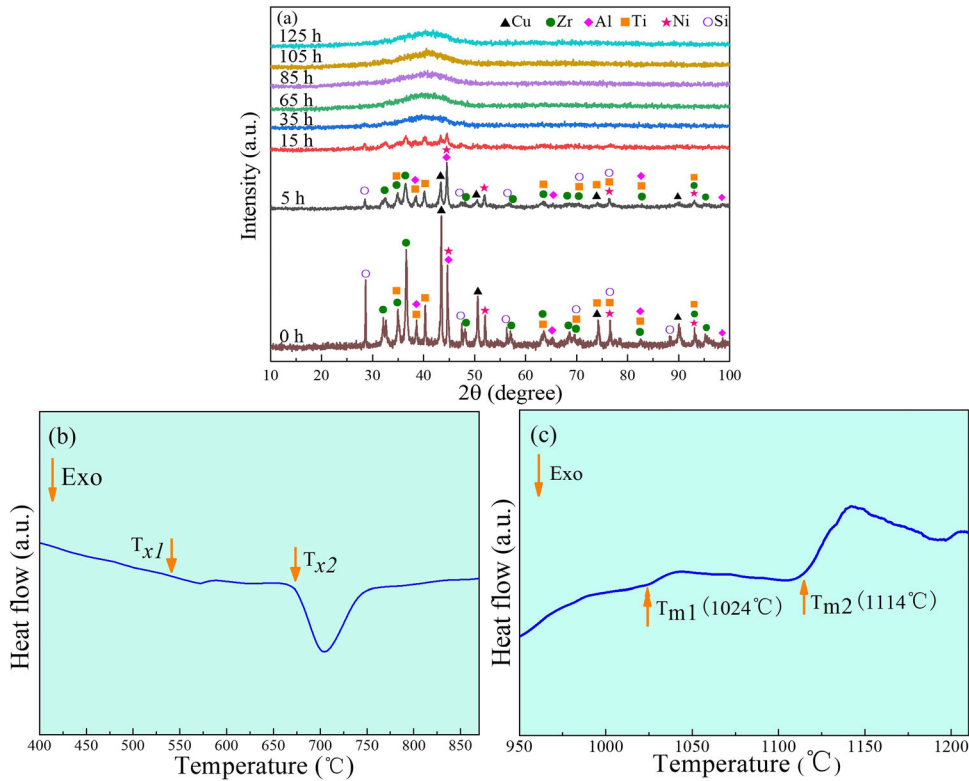


Fig. 1. XRD patterns of as-milled CuZrAlTiNiSi HEA powders after different milling times (a), and DSC curves after 125 h of milling time: 400–870°C (b); 950–1210°C (c).

requires the existence of chemical disordering, point defects, and lattice defects.¹² The accumulation of lattice defects could induce the crystal-to-amorphous phase transformation.¹³ Furthermore, the volume fraction of the formed HEA amorphous phase increases with increasing MA time.

From Fig. 1c, it can be observed that there are two endothermic peaks, revealing the two-step melting process. The melting temperatures, T_{m1} and T_{m2} , are 1024°C and 1114°C, respectively. Considering the sintering pressure and avoiding overheating during VHPS process, the sintering temperature was set to 930°C, which was lower than the T_{m1} of about 100°C.

The FESEM images and EDS spectrums of the as-milled powders after different milling time are presented in Fig. 2. The 15-h milled powder particles reveal the uneven shape and size (Fig. 2a). The larger and smaller sizes of the powder particles are about 70 μm and 20 μm , respectively. At this milling stage, an alloying reaction begins to occur according to the XRD curve (Fig. 1). The element powders with a brittle nature are easily fractured during ball milling, and are broken into smaller particles. Prolonging the milling time to 65 h, the edges of the powder particles exhibit an obvious refinement from irregular to regular round-shaped, as shown in Fig. 2b and b-1. The size of the powder particles of the 65-h milled HEA is reduced to less than 8 μm . After the milling time reaches 125 h

(Fig. 2c and c-1), there is no significant reduction in particle size. However, the particles become smoother, and are closer to a spherical shape compared with the 65-h milled powders. Moreover, compared with the EDS result of the 65-h milled powders, this shows that each principal element component in the 125-h milled powders possesses the more homogeneous distribution (Fig. 2d). However, a small amount of Fe element is found in the tested powders. The Fe content in the 15-milled powders is 1.49 at.%, which comes from the grinding ball and the grinding pot. With increasing the milling time from 65 h to 125 h, the Fe contents are 4.62 at.% and 5.11 at.%, respectively, indicating that the prolonged ball-milling treatment does not significantly enhance the iron pollution.

Figure 3 illustrates the XRD pattern of the CuZrAlTiNiSi HEAC. The inset shows the coating with a metallic sheen. The amorphous HEA phase tends to crystallize, and transforms to the complex crystalline phases during the hot sintering process. In combination with the EDS and elemental mappings described below, the phases in the coating are identified as face-centered cubic (FCC), body-centered cubic (BCC) solid solutions, some intermetallic compounds of β , Cr_3Si -type and Laves phases, and some unknown phases.

The FESEM images and elemental mappings of HEAC surface are shown in Fig. 4. The composition contents of different regions were detected by EDS

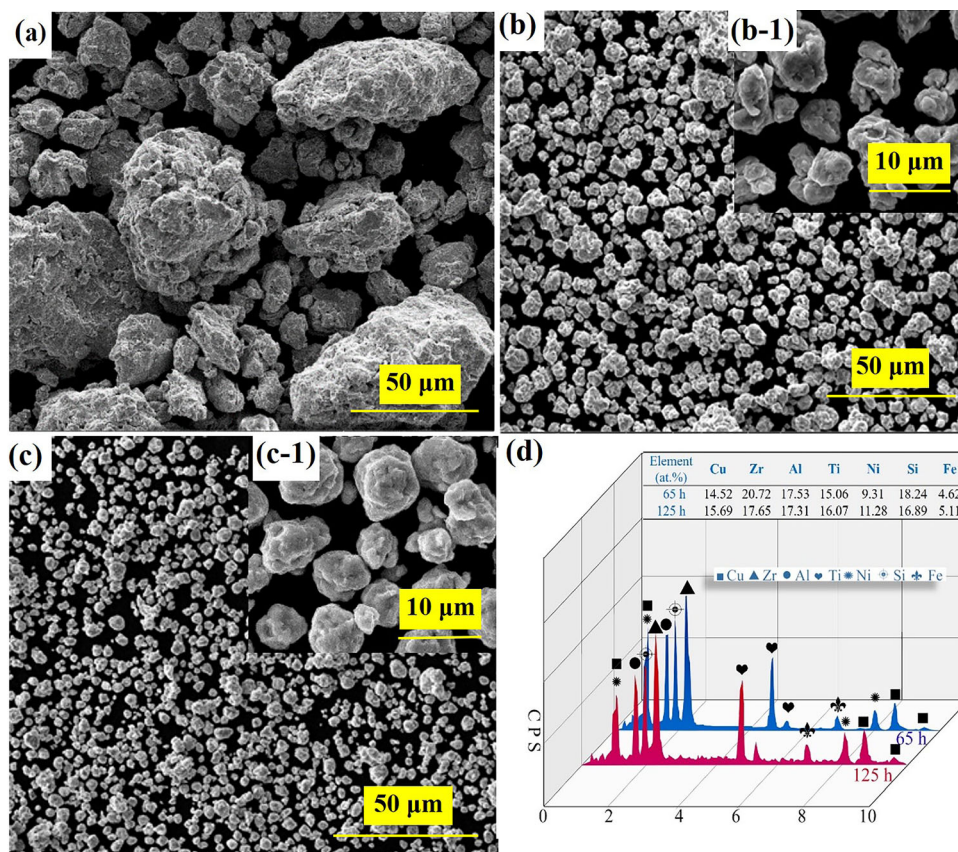


Fig. 2. FESEM images of the as-milled CuZrAlTiNiSi HEA powders after 15 h (a), 65 h (b) and 125 h (c) of milling time; EDS results of the as-milled powders after 65 h and 125 h of milling time (d).

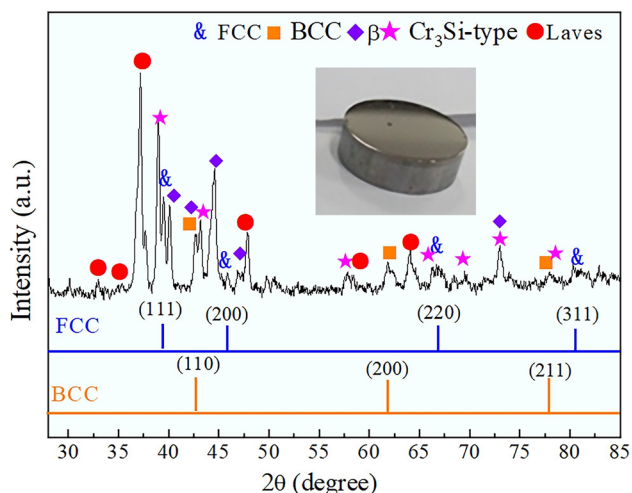


Fig. 3. XRD pattern of the CuZrAlTiNiSi HEAC, and inset of the sintered HEAC sample.

and are listed in Supplementary Table II. No pores and defects appear, suggesting a good consolidation quality of the coating, as shown in Fig. 4. The bright-gray phases with a width of about 1-2 μm (Region 1) exist in a network distribution, and can be regarded as the phase boundaries (Fig. 4a and b). According to the elemental mappings in Fig. 4d, g

and h, elements Si, Ni and Zr are mainly enriched at the phase boundaries. The composition contents reveal 26.7 at.% of Si, and 73.3 at.% of Zr, Ni and other elements (with low contents) in total (Supplementary Table II), which agrees well with the 1:3 stoichiometry of the Cr_3Si -type structure belonging to the topologically close-packed phase. Therefore, this phase can be called the $(\text{Zr}, \text{Ni})_3\text{Si}$ phase, in which Zr and Ni mainly share the Cr sites.

In Fig. 4b, it can be seen that there are several surrounded phases with different color contrasts and sizes, indicating the complex phase constitution. The compositions of the matrix in Region 2 are all Al-, Ti-, and Cu-rich, while there is a lack of Si and Ni elements. Two particle phases in nano-size are observed and uniformly distributed in the matrix. The sizes of dark (Region A) and grayish (Region B) particles are less than about 500 nm and 300 nm, respectively. The dark particles are mainly enriched with the Ti element, and are thought as the Ti-rich Laves phase combined with the XRD results. The grayish nano-sized phases consist of Al and Cu with the higher contents, and are considered as the β phase (AlCu_3 -type).

Figure 5 presents the FESEM image in cross-section and the corresponding elemental mappings. The Si and Zr elements mainly distribute in the

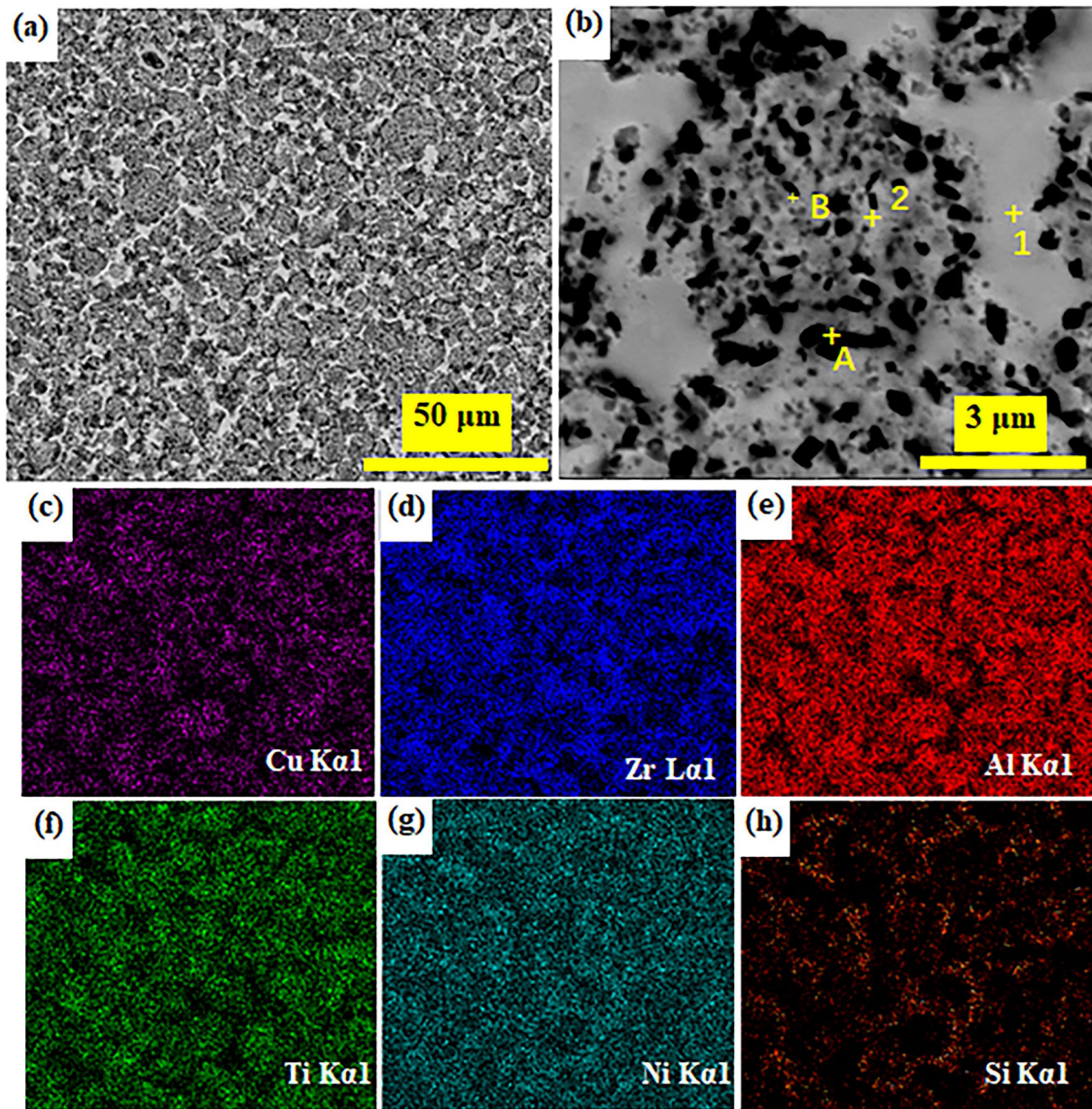


Fig. 4. FESEM morphologies of the CuZrAlTiNiSi HEAC surface (a) and (b), and the elemental mappings (c)–(h).

phase boundary, which corresponds well with the results of the EDS analysis. Moreover, it can be seen that the transition boundary is mainly rich in Ti. According to Supplementary Table II its corresponding Region 3 is mainly composed of the Ti element (85.9 at.%) and small quantities of Zr, Al and Fe. Interestingly, more Al atoms from the coating spread to the T10 steel substrate (14.1 at.% Al in Region 4), revealing the better diffusion ability, which is beneficial for enhancing the interface bonding between the coating and the substrate.

The values of structure entropy (S) has been calculated by the equation ($S = -R \sum_{i=1}^n c_i \ln c_i$)¹⁴ for the phases in Region 1 and Region 2. Where, R is the molar constant of the gas ($8.3145 \text{ J mol}^{-1} \text{ K}^{-1}$), c_i is the atomic percentage content of the i -th element. It is found that the values of S in Region 1 and Region 2 are 1.64R and 1.79R, which are

greater than the 1.61R in the range of high entropy.¹⁵ Although the sintered products contain two solid solutions and several intermetallic compounds, the VHPS-ed CuZrAlTiNiSi alloy is still in the high entropy region, and belongs to the HEA.

The microhardness distribution along the depth of the coating is shown in Fig. 6a. The average microhardness of the coating is around $927 \text{ HV}_{0.2}$, which is more than 3 times higher than that of the T10 substrate with $281 \text{ HV}_{0.2}$. In addition, the obtained microhardness of the coating is significantly higher than that of some HEACs containing the Si element which have been reported with less than 850 HV .^{16–18} Although the highest microhardness of the CuNiSiTiZr HEAC surface was more than 1000 HV , the microhardness near the substrate only reached about 500 HV .¹⁹ The tested coating in the present study bears the well-

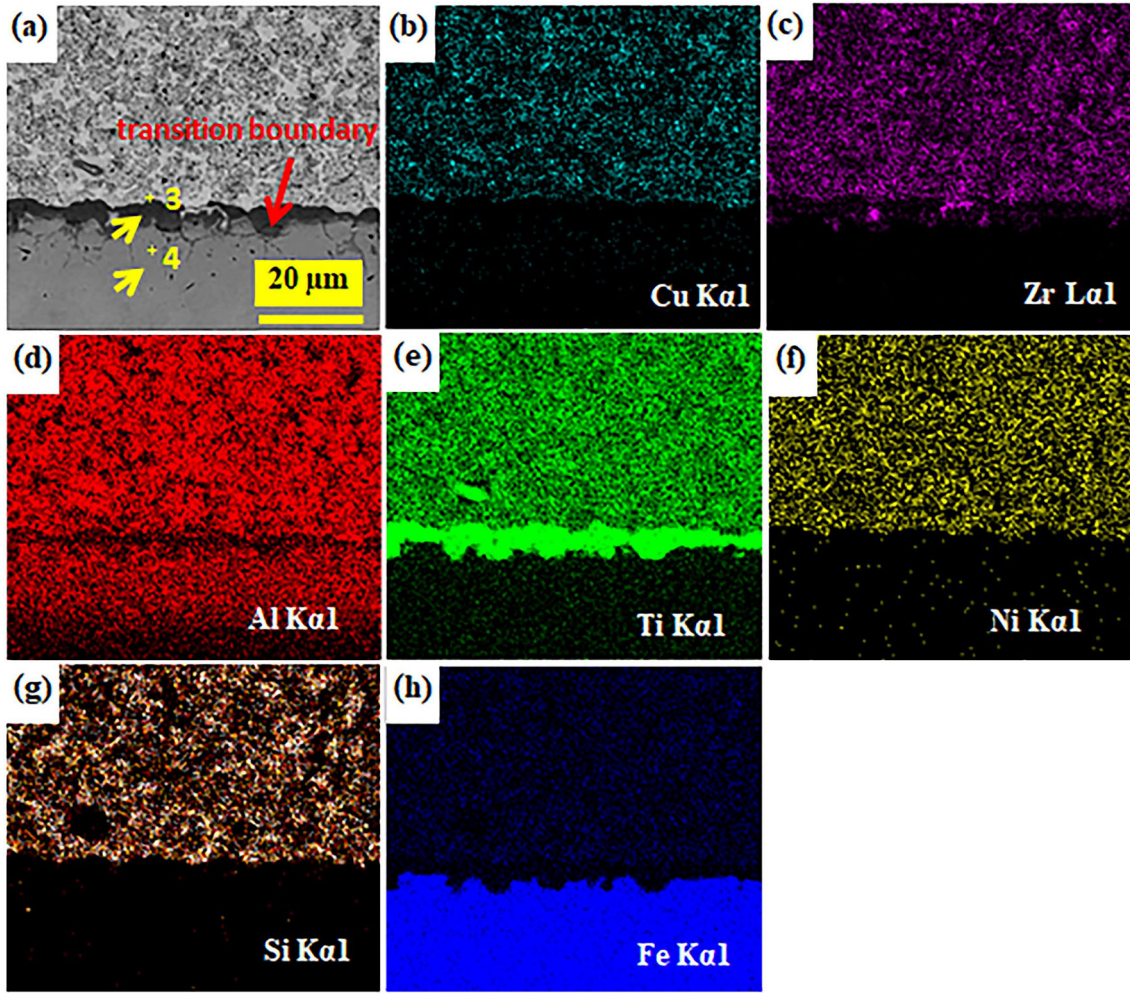


Fig. 5. FESEM morphology (a) of the CuZrAlTiNiSi HEAC in cross-sectional area, and the corresponding elemental mappings (b)-(h).

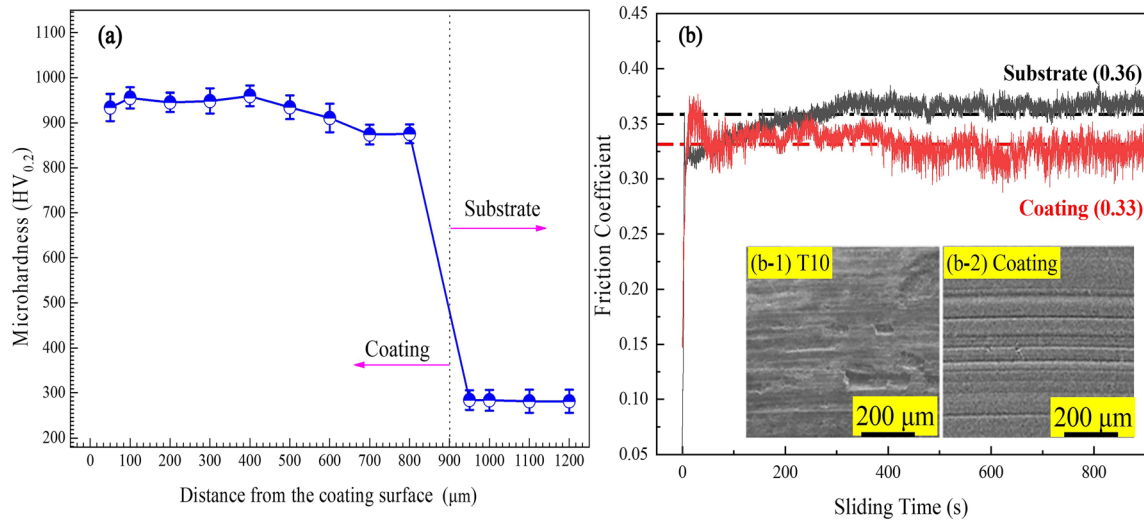


Fig. 6. Microhardness of the CuZrAlTiNiSi HEAC varies as the distance increased from the top surface to a depth of the substrate (a); variation of friction coefficients of the CuZrAlTiNiSi HEAC and T10 substrate (b) under linearly reciprocating friction; insets are morphologies of the worn surfaces of the T10 substrate (b-1) and coating (b-2).

distributed microhardness from the substrate to the coating surface (above 900 HV). The formation of the Cr_3Si -type phase in the sintered coating achieves the second phase strengthening effect, which accords with the results from Ren et al.²⁰ and Jin et al.²¹ They have reported that the Cr_3Si phase led to an increase in the hardness of the alloys. Moreover, according to the FESEM images, a large number of precipitated intermetallic compounds with sizes less than 500 nm are also beneficial to promote the effect of second phase strengthening. Compared with the other principal elements in HEAC, the addition of Si with the smallest atom size (0.11530 nm) can cause the larger atomic size mismatch in the lattice. The lattice strain (η) was calculated using the Williamson-Hall equation (Eq. 1) after eliminating the instrumental broadening.

$$B \cos \theta = \frac{0.89\lambda}{d} + \eta \sin \theta \quad (1)$$

where d is the crystallite size, λ is the wavelength of the X-radiation used (0.154056 nm), B is the full width at half maximum intensity, and θ is the Bragg angle.

The results show that the η values of the FCC and BCC phases in the CuZrAlTiNiSi HEAC are 0.48% and 0.98%, respectively. Compared to the CuZrAlTiNi HEAC free Si reported in our previous work,⁹ the calculated η values of the FCC (0.39%) and BCC (0.29%) phases are all lower than those of the CuZrAlTiNiSi HEAC. This shows that the existence of Si element causes more serious lattice distortion in the HEA, which can produce the higher stress field. It further increases the dislocation resistance, hinders its movement, and then enhances the deformation resistance of the matrix metal. Therefore, the obtained solid-solution strengthening effect can be implemented, and then the microhardness of the HEAC is improved. Combined with the excellent sintering quality, the above factors contribute to the hardness improvement of the CuZrAlTiNiSi HEAC.

Figure 6b reveals the variation of the friction coefficients of the CuZrAlTiNiSi HEAC and T10 substrate under linearly reciprocating friction. It shows that the friction coefficient of the coating (0.33) is slightly lower than that of the substrate (0.36). In addition, using other ring-disk friction and wear tests, the CuZrAlTiNiSi HEAC possesses the friction coefficient of 0.57 less than the T10 substrate (0.67), as shown in supplementary Fig. 1. The two methods of friction and wear tests both demonstrated that the CuZrAlTiNiSi HEAC exhibits good wear resistance with the lower friction coefficient. From the linear variation of friction coefficients for the tested samples (Fig. 6b), this shows an upward trend in the pre-friction period, owing to the change of the roughness of the worn contact surface. After a certain period of pre-grinding, the friction force and

the roughness of the grinding surface tend to be stable. The growth of the friction coefficient also becomes slow, and basically tends to be stable, thus entering the stable wear stage.²² Due to the low hardness of the T10 substrate, its worn surface has serious plastic deformation and material migration, revealing the serious peeling off of materials (Fig. 6 b-1). As shown in Fig. 6b-2, under the same conditions, the plastic deformation of the surface for HEAC is greatly reduced, and only a few furrows appear on the worn surface. All of these indicate that abrasive wear occurs on the surface of the CuZrAlTiNiSi HEAC.

In order to further identify the wear resistance of the HEAC and the substrate, 3D topography across the wear tracks is performed to measure the wear volume and specific wear rate. As can be clearly seen, the HEAC is effective in improving the wear resistance, based on the significant reduction of the wear groove depth and width (Fig. 7a). The wear volume and specific wear rate of the HEAC and the T10 substrate are shown in Fig. 7b.

The specific wear rate is defined in Eq. 2²³:

$$\text{Specific wear rate} = \frac{V}{FL} \quad (2)$$

where V is the wear volume, F is the normal load and L is the sliding distance. The smaller specific wear rate meant a higher wear resistance, because it removes the lower volume after sliding the same distance at the same normal load.²⁴ The wear volume of the coating and substrate is $8.79 \times 10^{-4} \text{ mm}^3$ and $937.10 \times 10^{-4} \text{ mm}^3$, respectively. Under the same friction conditions, the specific wear rate of the coating is only $0.45 \times 10^{-6} \text{ mm}^3/\text{N m}$, and it is also much lower than that of the substrate ($44.80 \times 10^{-6} \text{ mm}^3/\text{N m}$). The significant enhanced wear resistance of the HEAC might be attributed to the fact that the wear resistance is proportional to the alloy hardness, according to Archard's law.²⁵ Moreover, the mass wear rate of the counterbody can also characterize the wear resistance. The values of mass loss (m) of GCr15 steel after the coating and substrate wear tests (linearly reciprocating friction and wear tests) are about 0.3 mg and 0.4 mg, respectively. The mass wear rates (m/m_0) are only 0.3‰ and 0.4‰ for the tests of the HEAC and substrate, respectively. This further verifies that the HEAC possesses the better wear resistance.

The potentiodynamic polarization curves of the CuZrAlTiNiSi HEAC and the T10 substrate in a seawater solution are displayed in Fig. 8, which also shows the electrochemical parameters including corrosion potential (E_{corr}), pitting potential (E_{pit}), passivation current density (i_{pass}), and passive region ($\Delta E = E_{\text{pit}} - E_{\text{corr}}$). The corrosion current density (i_{corr}) cannot be directly determined because the coating and the T10 steel in this condition show a strong passivity with no clear Tafel region. Therefore, i_{corr} can be considered to be i_{pass} ,²⁶ which

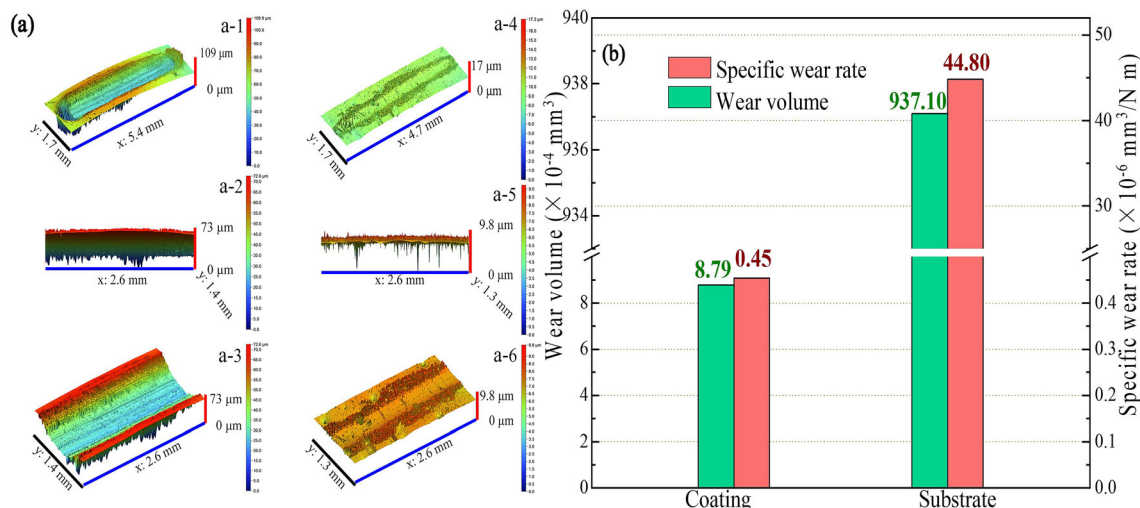


Fig. 7. White light interference pictures of the scratch in substrate ((a-1)-(a-3)) and coating ((a-4)-(a-6)); wear volume and specific wear rate of the HEAC and substrate (b).

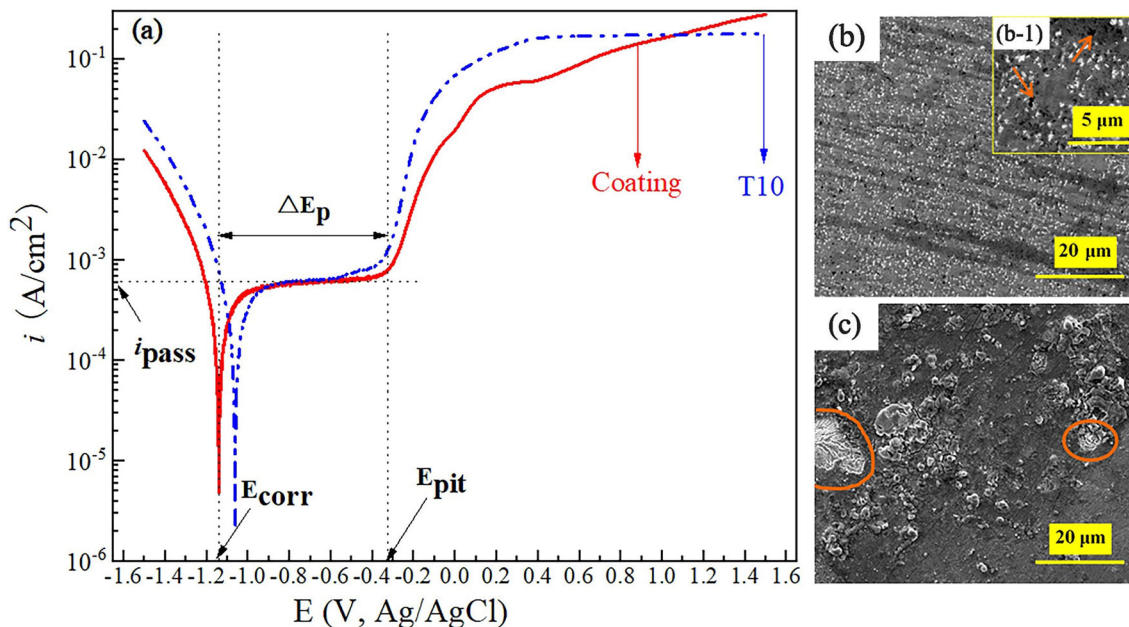


Fig. 8. Potentiodynamic polarization curves of the CuZrAlTiNiSi HEAC and T10 substrate (a); FESEM images of the HEAC ((b) and (b-1)) and T10 substrate (c) after the potentiodynamic polarization tests in seawater solution.

is $6.21 \times 10^{-4} \text{ A/cm}^2$ for the HEAC and $6.39 \times 10^{-4} \text{ A/cm}^2$ for the substrate. The coating and substrate show similar i_{corr} values. It is generally believed that the samples with high E_{corr} and low i_{corr} present good corrosion resistance.^{27,28} The HEAC has a small negative E_{corr} , indicating that its general corrosion resistance is slightly worse than that of the substrate in the seawater solution. However, the HEAC has the wider ΔE (0.83 V), which is far larger than that of the substrate (0.71 V), revealing the better pitting resistance.

To better compare the corrosion behavior of the HEAC and the T10 substrate, the surface morphologies of the samples corroded in the same conditions

were observed by FESEM (Fig. 8b and c). The surface morphology is uniform, and there is no rupture for the HEAC after polarization in seawater solution (Fig. 8b). A large number of light-white corrosion products less than about 600 nm in size are evenly dispersed at the surface, showing the uniform corrosion behavior. In addition, only a few tiny corrosion pits are observed on the passive film, as indicated by the arrows (Fig. 8b-1). The pitting corrosion is the local breakdown of the passive films with subsequent breakdown expansion, with fresh sections inside the pits being obtained. Therefore, This suggests that the passive film of the HEAC is relatively dense and not easy to break. However, the

corroded surface of the T10 substrate experiences extensive corrosion via chapping and shedding of the surface (Fig. 8c), along with some signs of microgalvanic corrosion (circled regions). The EDS mappings of the corrosion surface for the HEAC and the substrate are shown in supplementary Fig. 2. In addition to O-rich elements, the corrosion products deposited on the HEAC surface are mainly rich in Al, Ti and Cu (supplementary Fig. 2a). The relatively smooth surface without corrosion products mainly contains elements of Si, Ni and Zr, which is similar to the constitution proportion of the phase boundary characterized as the $(\text{Zr}, \text{Ni})_3\text{Si}$ phase. This indicates that the $(\text{Zr}, \text{Ni})_3\text{Si}$ phase does not react with Cl^- ions, demonstrating strong corrosion resistance. For the T10 steel substrate, the corroded surface is rich in Fe and O, as well as small amounts of Si and Mn, as shown in supplementary Fig. 2b. There are no obvious corrosion products. Thus, this further suggests that the HEAC displays better pitting resistance in the seawater solution than the substrate. Al and Ni atoms in the HEAC are likely to be attacked by the Cl^- ions, and readily form the Al_2O_3 and NiO passive films to provide good protection. Moreover, the Zr atoms also tend to participate in the anodic passivation, which promotes the formation of a protective film composed of ZrO_2 as well as $\text{Zr}(\text{OH})_4$.^{29,30} Compared with T10 steel, all of these factors can enhance the pitting resistance of the HEAC.

CONCLUSION

A CuZrAlTiNiSi HEAC with good consolidation quality was synthesized on a T10 substrate using MA and VHPS techniques. The results show that the final product of 125-h milled powders is an amorphous HEA phase, and that the sintered coating is mainly composed of two solid solutions and several intermetallic compounds. This reveals that the (Al, Cu, Ti)-rich phases in nano-size are precipitated from the solid-solution matrix. The HEAC bears a good sintering quality without pores and defects, as well as a good interface bonding between the coating and the substrate, which can be ascribed to the diffusion of Al atoms. The average microhardness of the coating reaches 927 $\text{HV}_{0.2}$, which is more than 3 times higher than the substrate. Besides the compact structures, the second phase strengthening and solid-solution strengthening are mainly beneficial for promoting the microhardness. The wear volume and the specific wear rate of HEAC are $8.79 \times 10^{-4} \text{ mm}^3/\text{Nm}$ and $0.45 \times 10^{-6} \text{ mm}^3/\text{Nm}$, which are much lower than those of the substrate. Combined with the reduction of the wear groove depth and width and the lower friction coefficient, this suggests that there was a significant improvement in the wear resistance of the HEAC. Furthermore, the coating

possesses the better pitting resistance in the seawater solution, characterized by the wider ΔE and uniform corrosion surface.

ACKNOWLEDGEMENTS

The authors acknowledge financial support from the National Natural Science Foundation of China (Nos. 51671095 and 51971102).

ELECTRONIC SUPPLEMENTARY MATERIAL

The online version of this article (<https://doi.org/10.1007/s11837-020-04005-x>) contains supplementary material, which is available to authorized users.

REFERENCES

1. Y. Zhang, T.T. Zuo, Z. Tang, M.C. Gao, K.A. Dahmen, P.K. Liaw, and Z.P. Lu, *Mater. Sci.* 61, 1 (2014).
2. K.Y. Tsai, M.H. Tsai, and J.W. Yeh, *Acta Mater.* 61, 4887 (2013).
3. Y.P. Lu, X.Z. Gao, L. Jiang, Z.N. Chen, T.M. Wang, J.C. Jie, H.J. Kang, Y.B. Zhang, S. Guo, H.H. Ruan, Y.H. Zhao, Z.Q. Cao, and T.J. Li, *Acta Mater.* 124, 143 (2017).
4. Q.Y. Zhou, S. Sheikh, P. Ou, D.C. Chen, Q. Hu, and S. Guo, *Electrochem. Commun.* 98, 63 (2019).
5. M.G. Poletti, G. Fiore, F. Gili, D. Mangherini, and L. Battezzati, *Mater. Des.* 115, 247 (2017).
6. X.W. Qiu, Y.P. Zhang, and C.G. Liu, *J. Alloys Compd.* 585, 282 (2014).
7. J.B. Cheng, X.B. Liang, and B.S. Xu, *Surf. Coat. Technol.* 240, 184 (2014).
8. N. Tüten, D. Canadinc, A. Motallebzadeh, and B. Bal, *Intermetallics* 105, 99 (2019).
9. W.J. Ge, B. Wu, S.R. Wang, S. Xu, C.Y. Shang, Z.T. Zhang, and Y. Wang, *Adv. Powder Technol.* 28, 2556 (2017).
10. C.Y. Shang, E. Axinte, J. Sun, X.T. Li, P. Li, J.W. Du, P.C. Qiao, and Y. Wang, *Mater. Des.* 117, 193 (2017).
11. Y. Wang, H.R. Geng, Z.X. Yang, X.Y. Teng, and G.R. Zhou, *J. Non-Cryst. Solids* 354, 3984 (2008).
12. M.S. El-Eskandarany, J. Saida, and A. Inoue, *Acta Mater.* 51, 4519 (2003).
13. V.A. Palvov, *Phys. Met. Metallovd.* 59, 1 (1985).
14. T.B. Massalski, *Mater. Trans.* 51, 583 (2010).
15. J.Y. Yeh, Y.L. Chen, and S.J. Lin, *Trans. Technol. Publ.* 560, 1 (2007).
16. H. Zhang, Y. Pan, Y.Z. He, and H.S. Jiao, *Appl. Surf. Sci.* 257, 2259 (2011).
17. H. Zhang, Y. Pan, and Y.Z. He, *Mater. Des.* 32, 1910 (2011).
18. B.Q. Wu, H.C. Rao, C. Zhang, and P.Q. Dai, *Surf. Technol.* 44, 85 (2015).
19. X.R. Wang, Z.Q. Wang, P. He, T.S. Lin, and Y. Shi, *Surf. Coat. Technol.* 283, 156 (2015).
20. B. Ren, R.F. Zhao, Z.X. Liu, S.K. Guan, and H.S. Zhang, *Rare Met.* 33, 149 (2014).
21. B.Q. Jin, N.N. Zhang, S. Guan, Y. Zhang, and D.Y. Li, *Surf. Coat. Technol.* 349, 867 (2018).
22. S. Liang, P. Zhu, Y. Yang, X. He, W.R. Wang, and X.C. Wei, *Tribol. Lett.* 67, 102 (2019).
23. C. Huang, Y.Z. Zhang, R. Vilar, and J.Y. Shen, *Mater. Des.* 41, 338 (2012).
24. C.L. Wu, S. Zhang, C.H. Zhang, H. Zhang, and S.Y. Dong, *Surf. Coat. Technol.* 315, 368 (2017).

25. Y. Zhang, T.T. Zuo, Y.Q. Cheng, and P.K. Liaw, *Sci. Rep.* 3, 1455 (2013).
26. R. Jindal, V.S. Raja, M.A. Gibson, M.J. Styles, T.J. Bastow, and C.R. Hutchinson, *Corros. Sci.* 84, 54 (2014).
27. X.F. Wang, X.Q. Wu, J.G. Lin, and M. Ma, *Mater. Lett.* 61, 1715 (2007).
28. J.G. Lin, W.W. Wang, X.Q. Wu, J.H. Lei, and S. Yin, *J. Alloys Compd.* 478, 763 (2009).
29. L.X. Zhang, B.Y. Li, H. Wu, W. Wang, S.C. Zhai, J. Xu, Z.Z. Niu, and Y. Wang, *Adv. Powder Technol.* 29, 1695 (2018).
30. D. Zander and U.K. Zan, *Mater. Sci. Eng. A* 375, 53 (2004).

Publisher's Note Springer Nature remains neutral with regard to jurisdictional claims in published maps and institutional affiliations.